First Investigation of the Relationship Between Solar-Induced Chlorophyll Fluorescence Observed by TanSat and Gross Primary Productivity

Shanshan Du, Liangyun Liu, Xinjie Liu, and Jidai Chen

***Abstract*—Reliable estimation of gross primary production (GPP) of terrestrial ecosystems is crucial in the global carbon cycle and ecosystem functioning studies. Solar-induced chlorophyll fluorescence (SIF) has emerged as an unprecedented proxy for terrestrial GPP estimation. TanSat SIF with a 2-km fine spatial resolution provides an excellent opportunity to investigate the relationships of satellite SIF and eddy covariance (EC) GPP at ecosystem or site scale, while has not been investigated. In this article, we investigated the relationship between TanSat SIF and EC GPP based on flux tower sites encompassing different biomes over the globe. TanSat SIF exhibited strong relationships with EC GPP at Fe and KI bands for instantaneous and daily timescales. The correlations between EC GPP and TanSat SIF ($R^2 = 0.61$) were much better than moderate resolution imaging spectroradiometer (MODIS) bidirectional reflectance distribution function (BRDF)-corrected vegetation indices (VIs) ($R^2 = 0.48$–0.58). Further comparisons between SIF and GPP with absorbed photosynthetically active radiation (APAR) and two environmental factors (fTmin and fVPD) showed that SIF responded to APAR and was similarly affected by environmental factors as GPP. GPP derived from SIF ($R^2 = 0.64$) also performed slightly better than enhanced vegetation index and near-infrared reflectance of vegetation and even light use efficiency MODIS GPP algorithm ($R^2 = 0.58$–0.60). Therefore, our results demonstrated the feasibility of SIF on estimating GPP at sites or ecosystem levels; in addition, incorporating TanSat SIF with other satellite SIF products will open a new era for carbon cycling and ecosystem functioning studies.**

***Index Terms*—Gross primary productivity, moderate resolution imaging spectroradiometer (MODIS), solar-induced chlorophyll fluorescence (SIF), tanSat.**

I. Introduction

ESTIMATING terrestrial vegetation photosynthesis is significant in understanding the global carbon cycle and monitoring ecosystem productivity [1]–[3]. Reflectance-based vegetation indices (VIs), such as normalized difference vegetation index (NDVI) and enhanced vegetation index (EVI), are widely used in regional and global vegetation gross primary productivity (GPP) estimation [4]–[6]. However, reflectance-based VIs can only reflect vegetation canopy structure variations; they cannot reveal a photosynthetic capacity, which shows large uncertainties on a small temporal scale and interannual variations [7]. Over the past decade, solar-induced chlorophyll fluorescence (SIF) has been deemed as an alternative proxy for estimating terrestrial GPP due to its close link to photosynthesis [8]–[11]. SIF is essentially an energy flux emitted by plant chlorophyll molecules under natural sunlight, which covers the wavelength range of ∼650–800 nm, with two peaks at ∼683 and 740 nm. Three different pathways are mainly included when plant chlorophyll molecules absorb light energy: nonphotochemical quenching, photochemistry, and re-emitted as SIF [12], [13]. Consequently, compared with the traditional VIs, SIF shows a close physiological correlation with the photosynthesis status of vegetation [14], [15].

Although numerous studies have demonstrated the significant relationships between SIF and GPP at different spatial and temporal scales using ground-based [8], [16]–[20], airborne-based, and space-borne [9], [11], [21]–[24] remotely sensed SIF observations with gridded GPP or eddy covariance (EC) tower-based GPP measurements, directly employing SIF to estimate global GPP is still challenging. Generally, most ecosystems are homogeneous at the limited spatial scales of hundreds of meters or a few kilometers [25], [26]. The effects of vegetation ecosystem, plant biomes, canopy structure, and even bioclimatic factors on the relationships between SIF and GPP at different temporal and spatial scales require in-depth investigation. To date, numerous atmospheric satellites or sensors have emerged with the potential of global SIF observations from space. Previous studies have successfully obtained global satellite-derived SIF measurements based on the Global Ozone Monitoring Experiment-2 (GOME-2) [27], [28], SCanning Imaging Absorption spectrometer for Atmospheric CHartographY (SCIAMACHY) [29], [30] and Greenhouse Gases Observing Satellite (GOSAT) [31]–[33] observations. However, the coarse spatial resolution of these SIF measurements has hindered GPP evaluation using SIF as there is a spatial mismatch between the observation footprints of a satellite and EC tower. The launch of TROPOspheric Monitoring Instrument (TROPOMI) [34]–[36] (3.5 km × 7 km) and Orbiting Carbon Observatory (OCO-2)

Manuscript received August 11, 2021; revised October 17, 2021 and November 10, 2021; accepted November 12, 2021. Date of publication November 16, 2021; date of current version December 2, 2021. This work was supported in part by the Key Research Program of the Chinese Academy of Sciences under Grant ZDRW-ZS-2019-1, in part by the National Key Research and Development Program of China under Grant 2017YFA0603001 and in part by the National Natural Science Foundation of China under Grant 41871239. *(Corresponding author: Liangyun Liu.)*

The authors are with the Aerospace Information Research Institute, Chinese Academy of Sciences, Beijing 100094, China (e-mail: duss@radi.ac.cn; liuly@radi.ac.cn; liuxj@radi.ac.cn; chenjidai@aircas.ac.cn).

This article has supplementary downloadable material available at https://doi.org/10.1109/JSTARS.2021.3128355, provided by the authors.

Digital Object Identifier 10.1109/JSTARS.2021.3128355

This work is licensed under a Creative Commons Attribution 4.0 License. For more information, see https://creativecommons.org/licenses/by/4.0/

[37], [38] (1.3 km × 2.25 km) features a much smaller spatial resolution to compare and validate the EC tower-based GPP with satellite-derived SIF measurements. Besides, Chinese Carbon Dioxide Observation Satellite Mission (TanSat), launched on December 21, 2016, also provides unprecedented prospects in comparing satellite-based SIF with ground-based GPP measurements at the ecosystem scale with a significantly comparable spatial resolution (2 km × 2 km) [39], [40]. Numerous studies have investigated the relationships between OCO-2 SIF and EC GPP measurements [41]–[43], whereas there are rarely relative studies on TanSat SIF products. The mismatched resolution between EC flux and space SIF is still the key problem in conducting research GPP with SIF. However, only OCO-2 SIF has comparable resolution with EC flux towers currently. In this context, TanSat SIF observations opened up a new perspective on investigating the mechanism link between satellite-based SIF and EC flux GPP measurements benefiting from the consistency of footprint size with flux towers. Furthermore, investigating the relationships between TanSat SIF and EC GPP will be useful for monitoring vegetation photosynthetic activity and carbon cycling at large scales by incorporating other satellite SIF products.

TanSat is the first Chinese satellite dedicated to accurately estimating carbon dioxide (CO_2) concentration at regional to continental scales. The high spectral resolution (∼0.044 nm) at the O_2-A band makes it possible to retrieve SIF products [44]. TanSat strategized three modes of observations—nadir, glint, and target modes—and a revisit period of 16 days. However, because of the strong Doppler shifts in the glint mode and the rarely small number of observations in the target mode, successful retrievals of SIF have only been conducted in the nadir modes. As a result, the TanSat SIF products covering the period from March 2017 to October 2019 for nadir mode have been obtained [39]. Nevertheless, TanSat has not been successfully operated since November 2019 due to the error of the satellite module.

In this article, we present the first investigation of the performance of the TanSat SIF dataset on GPP estimation using observations on various terrestrial vegetation biomes and assess how this relationship varied with different vegetation biomes. We collected EC flux observations of 203 flux sites and identified an EC dataset of 129 sites with concurrent TanSat coverage. First, we examined the relationships between TanSat SIF and EC GPP at Fe and KI bands for instantaneous and daily timescales. Second, we compared the correlations between EC GPP and TanSat SIF with moderate resolution imaging spectroradiometer (MODIS)-derived bidirectional reflectance distribution function (BRDF)-corrected VIs, including NDVI, EVI, and near-infrared reflectance of vegetation (NIR_v). Third, to further investigate the link between SIF and GPP, we evaluated the responses of SIF and GPP to photosynthetically active radiation (PAR), absorbed PAR (APAR), the fraction of APAR (FAPAR), and the product of APAR and two environmental factors, i.e., fTmin and fVPD. Finally, the performances of estimated GPP based on SIF, VIs, and light use efficiency (LUE) MODIS GPP algorithm were compared.

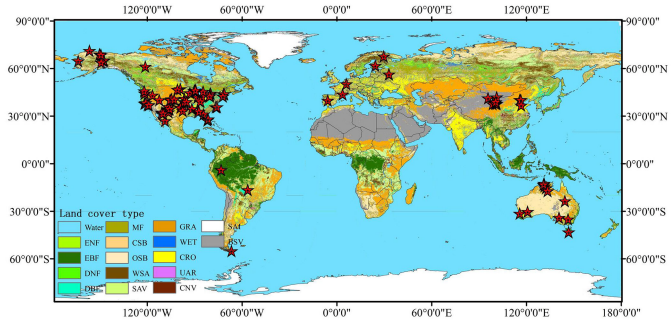

Fig. 1. EC flux site distribution. The land cover map is derived from the MODIS land cover type product (MCD12Q1) based on International Geosphere–Biosphere Programme (IGBP) classification scheme. CRO = the cropland type, GRA = grasslands type, DBF = decious broadleaf forests, ENF = evergreen needleleaf forests type, OSH = open shrublands type, SAV = savannas type, WSA = woody savannas type, MF = mixed forests type, WET = wetlands type, and BSV = bare or sparsely vegetated type.

II. Materials and Methods

A. Site Descriptions

A total of 203 EC flux sites across the globe were screened to match the synchronous observations of TanSat and flux tower measurements from March 2017 to October 2019. For each site, a search range of ∼5 km × 5 km was exploited to search the observations that TanSat overpasses the EC flux towers. TanSat operates a revisit period of 16 days and it cannot acquire the global continuous imager, which results in highly limited daily coverages especially under a single observation mode. Consequently, the availability of synchronous observations of TanSat surrounding flux sites within 5 km was largely constrained. There were no TanSat overpasses within the search range of 5 km surrounding the flux tower for part of EC flux sites. For some EC flux sites, there were one or few more observations of TanSat overpasses; meanwhile, on the one hand, concurrent flux measurements were observed or shared, on the other hand, no successfully retrieved SIF signals were obtained due to the quality of TanSat spectrum measurements. Besides, some highly heterogeneous flux sites were excluded according to the MODIS land cover data. Ultimately, 129 EC flux sites were selected, which included both flux measurements and TanSat SIF retrievals, and a number range from 1 to 7 of successfully retrieved SIF footprints of TanSat encompassing each flux site was identified. Fig. 1 depicts the 129 selected EC flux site distribution having TanSat SIF overpasses. Nine major vegetation biome types were encompassed by the selected flux sites: 14 cropland (CRO), 31 grassland (GRA), 15 deciduous broadleaf forest (DBF), 27 evergreen needle leaf forest (ENF), 8 open shrubland (OSH), 9 savanna (SAV), 7 woody savanna (WSA), 9 mixed forest (MF), and 9 wetlands (WET) sites. Detailed information, including the site ID, name, latitude, longitude, biome type, and the number of TanSat SIF, overpasses are summarized in Table SI in Supplementary Material. The average time of successfully retrieved TanSat SIF encompassing each site was ∼2.3 from March 2017 to October 2019.

B. EC Flux Data

EC systems, comprising a 3-D sonic anemometer to measure 3-D velocity and temperature and an open path infrared CO_2/H_2O gas analyzer to measure CO_2 and H_2O density, and an automatic weather station were used to measure the flux exchange between the ecosystem and atmosphere, as well as meteorological variables for each EC flux site [45]. Raw EC data with a 10-Hz sampling frequency were postprocessed to high-quality flux data with a 30-min interval after data filtering using EddyPro software [46]–[48]. Online tools available on the Max Planck Institute for Biogeochemistry's website[1] were exploited to calculate GPP after conducting the gap-filling and flux partitioning processes. In these processes, GPP data based on nighttime and daytime partitioning [49], [50] approaches were calculated. However, GPP data based on the nighttime approach were not successfully calculated for some sites due to the poor quality of vapor pressure deficit and temperature measurements. A previous study has demonstrated that the difference in GPP estimations using 23 different flux partitioning methods was less than 10% [51]. Therefore, to make exploit the EC flux dataset, GPP estimation based on daytime partitioning algorithm was used in this study.

C. TanSat SIF Data

TanSat SIF product was employed to investigate the relationship between satellite-derived SIF and EC GPP data. TanSat SIF data were retrieved using level 1B radiance data of O_2-A band derived by Atmospheric Carbon dioxide Grating Spectrometer (ACGS) maintained at the National Satellite Meteorological Center, China Meteorological Administration [39]. Two far-red SIF data at 758 and 771 nm (hereinafter, SIF_{Fe} and SIF_{KI}, respectively) retrieved using a data-driven algorithm accompanied by an auxiliary geometrical dataset were included in the SIF product. In addition, owing to the poor quality of spectrum measurements of O_2-A band in the glint mode, only SIF data in the nadir mode were successfully retrieved. Besides the instantaneous values of SIF at ∼13:30 local time, daily SIF values could also be available making use of the daily mean factor calculated based on the strong correlation between PAR and solar zenith angle [38], [39]. Furthermore, the daily correction factors were provided in the public TanSat SIF dataset [39]. Eventually, to maintain the available amount of TanSat SIF soundings surrounding EC sites and decrease the influence of heterogeneous land surface of EC sites, TanSat SIF soundings were extracted within 5 km from each flux tower. Owing to the smaller spatial resolution of 2 km for TanSat, TanSat SIF soundings with the same land cover type for each site within 5 km were finally selected and directly averaged, which was to maintain consistency between TanSat SIF soundings and flux sites. On the one hand, most EC sites are homogeneous at the limited spatial scales of hundreds of meters or a few kilometers, which depends on the height of EC towers. On the other hand, the highly heterogeneous flux sites were rejected in this article.

[1][Online]. Available: https://www.bgcjena.mpg.de/bgi/index.php/Services/REddyProcWeb

D. MODIS Products

Three MODIS-derived satellite products with a 500-m spatial resolution were employed in this study; they were obtained from the NASA Level-1 and Atmosphere Archive and Distribution System Distributed Active Archive Center (LAADS DAAC). To distinguish the heterogeneities around available sites, the MODIS land cover product (MCD12Q1) and IGBP classification scheme were used as criteria for discrimination. Two MODIS reflectance products, including daily nadir BRDF-adjusted reflectance product, MCD43A4, and Aqua reflectance product, MYD09GA, were used to derive NDVI, EVI, and NIR_v for comparisons. A 4-day composite FPAR dataset, MCD15A3H, was also used to calculate the tower-based APAR based on flux PAR measurements for further comparisons with SIF and GPP.

E. Statistical Analysis

First, we evaluated the relationship of TanSat SIF and EC GPP at both Fe and KI bands for instantaneous and daily timescales using the 129 EC site observations. Almost all EC flux sites had half-hourly GPP data, whereas two sites (US-MMS and US-Ne1) only provided hourly GPP data. To match the equator crossing time of TanSat, the instantaneous GPP data were extracted from the half-hourly averaged values from 1:00 to 1:30 P.M. for almost all sites and the hourly data were interpolated to obtain the midday instantaneous GPP observations for the sites. Meanwhile, three VIs, MODIS-derived NDVI, EVI, and NIR_v, were compared with EC GPP and TanSat SIF. The VIs were calculated from two MODIS-derived reflectance products for the days having TanSat SIF. In addition, to investigate whether the SIF–GPP relationships differed across vegetation biomes, which had been reported in previous studies [9], [21], [52], the selected global EC measurements were separately used to fit the SIF–GPP relationship for each biome and the differences in the slopes of the SIF–GPP relationships were examined. As for the selection of EC sites, two steps were conducted on determining whether a site should be retained or rejected. First, a site that had concurrent TanSat SIF soundings and GPP observations could be retained. Second, Shannon's Diversity Index (SHDI, less than 2.10), calculated based on the IGBP land cover product of MCD12Q1 dataset, was used to determine whether a site should be retained or rejected. Then, we analyzed the relationships between SIF at Fe band, EC GPP and PAR, FAPAR, APAR. Furthermore, two environmental factors, i.e., fTmin and fVPD, used in MODIS GPP estimations based on the LUE model were multiplied by APAR for comparison with TanSat SIF and EC GPP. Two environmental factors were derived from the meteorological observations.

Finally, to investigate whether SIF had advantages on GPP estimations, the GPP estimate from TanSat SIF was comparable to those from MODIS EVI, NIR_v, and EC GPP and LUE-based MODIS GPP algorithm using all the concurrent TanSat SIF and EC site observations for all biomes. For SIF and VIs methods, *K*-fold cross-validation was carried out to assess the performances of estimating GPP. Considering the amount of the dataset, we set *K* as 10 in this study, i.e., the fitting processes were all performed

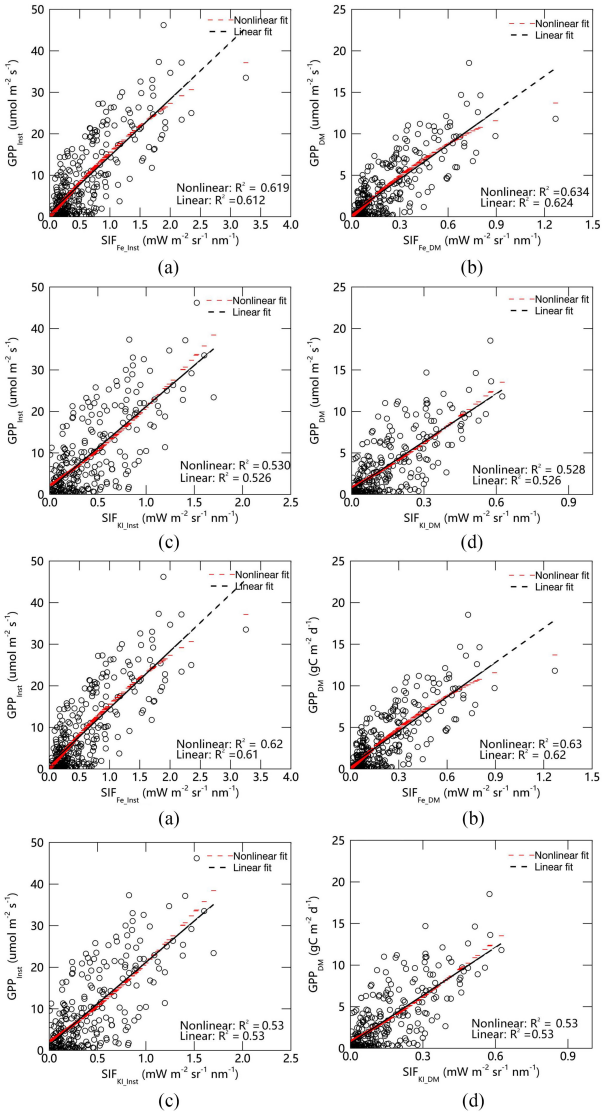

Fig. 2. Relationships between (a) and (b) TanSat SIF and EC GPP at Fe and (c) and (d) KI bands for instantaneous (a) and (b) and daily (b) and (d) timescales.

10 times; then, the averaged fitted GPP was regarded as the final fitted GPP to compare with true EC GPP values. We employed the coefficient of determination (R^2) and root-mean-square error (RMSE) to evaluate their predictive abilities.

III. Results

A. Comparisons Between TanSat SIF and VIs With EC GPP

As shown in Fig. 2, strong linear relationships between TanSat SIF and flux tower GPP were observed at Fe and KI bands regardless of the timescale, which showed that the correlations between TanSat SIF and GPP were better at Fe band ($R^2 = 0.61$ for $\mathrm{SIF_{Inst}}$ and $R^2 = 0.62$ for $\mathrm{SIF_{DM}}$) than at KI band ($R^2 = 0.53$ for $\mathrm{SIF_{Inst}}$ and $R^2 = 0.53$ for $\mathrm{SIF_{DM}}$) for both timescales. Meanwhile, no obvious advantages of goodness-of-fit for daily scale compared with that for instantaneous scale was observed, especially for KI band. Moreover, it can be found that the accuracy of nonlinear

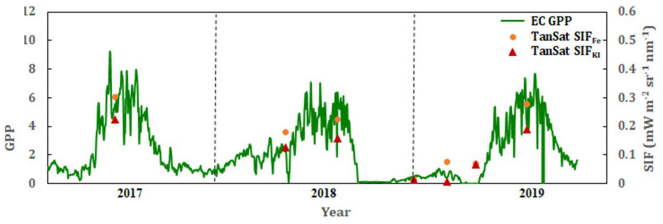

Fig. 3. Seasonal trajectories of GPP and daily TanSat SIF at an EC grassland site (CN-SDQ) from March 1, 2017 to October 31, 2019.

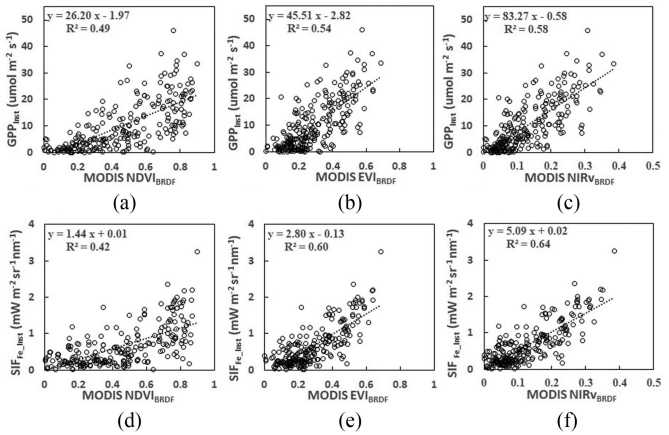

Fig. 4. Relationships between MODIS BRDF-corrected NDVI, EVI, and $\mathrm{NIR_V}$ derived from MCD43A4 reflectance product with (a)–(c) EC GPP and (d)–(f) TanSat SIF, respectively.

(hyperbolic) models had no obvious differences compared with that of a linear model for both bands and timescales.

Fig. 3 illustrated the seasonal trajectories of EC GPP and TanSat SIF at Sidaoqiao (CN-SDQ) site, which has a relative frequent visit with seven valid soundings. CN-SDQ site is located along the lower reaches of the Heihe hydrometeorological observation network in Sidao Bridge, Ejina Banner, Inner Mongolia, China (101.14° E, 42.00° N). Although the amount of available concurrent TanSat SIF and EC GPP samples was very limited, they covered different grassland growing period of site CN-SDQ except for the late growing stage. We found that TanSat-derived SIF at both Fe and KI band well tracked the seasonal cycle of EC GPP, which indicates the potential of satellite-derived SIF on estimating GPP.

To help assess the feasibility of TanSat SIF for estimating GPP, further comparisons between three VIs, NDVI, EVI, and $\mathrm{NIR_V}$, derived from MODIS BRDF-corrected reflectance products with EC GPP and TanSat SIF at Fe band were first examined (see Fig. 4). Overall, strong relationships between VIs and EC GPP were observed with values of R^2 ranging from 0.49 to 0.58. $\mathrm{NIR_V}$ performed best on interpreting GPP, whereas NDVI showed the weakest correlation with EC GPP among three VIs. Nevertheless, the relationship between $\mathrm{NIR_V}$ and EC GPP ($\mathbf{R^2} = 0.58$) was still weaker than that between TanSat SIF and EC GPP ($\mathbf{R^2} = 0.61$). We also compared VIs with TanSat SIF at Fe band in Fig. 4. Similarly, $\mathrm{NIR_V}$ ($\mathbf{R^2} = 0.64$) had the strongest correlation with SIF than EVI ($\mathbf{R^2} = 0.60$) and NDVI ($\mathbf{R^2} = 0.42$). In addition, EVI and $\mathrm{NIR_V}$ showed much stronger correlations with

SIF than with GPP. Owing to the NDVI saturation at high values, the correlations between NDVI with GPP and SIF were discrete. Therefore, EVI and NIR_v correlated more with GPP or SIF than NDVI. Meanwhile, to make a strict analysis on matching TanSat SIF and MODIS VIs according to the overpassing time of TanSat, we also compared these three VIs derived from Aqua MODIS reflectance product (MYD09GA) with EC GPP and TanSat SIF, as illustrated in Fig. S1. The results showed that EC GPP or TanSat SIF exhibited much stronger correlations with VIs derived from the BRDF-corrected reflectance than that based on Aqua product. This indicated that the varying observation geometry could strongly affect the reflectance of an object on the Earth, which will also affect the reflectance-derived VIs, especially for NDVI.

B. Relationships Between TanSat SIF and GPP With APAR

To further investigate the link between TanSat SIF and EC GPP, we assessed the relationships between SIF and GPP with PAR, FAPAR, APAR, and APAR $fT_{min} \times fVPD$ (see Fig. 5). It showed that PAR, FAPAR, and APAR explained 13%, 45%, and 59% of the variance in SIF at Fe band and 11%, 53%, and 60% of the variance in EC GPP. Discrete scatters were found between SIF, GPP, and PAR. APAR, the product of PAR and FAPAR, explained much more variance in both SIF and GPP than PAR or FAPAR alone. In addition, the correlations between pairs of SIF, GPP, and APAR tended to linearize and converge, which indicated that SIF and GPP mainly depend on APAR, resulting in the strong link between SIF and GPP. Furthermore, the product of APAR and environmental scaling factors derived from two simultaneous meteorological measurements was employed for comparisons with TanSat SIF and EC GPP. As shown in Fig. 5, except for APAR, other environmental factors will also influence SIF and GPP. However, GPP was much more influenced by environmental factors than SIF, attributable to the effects of environmental factors on photosynthetic LUE (LUE_p).

To make further comparisons between VIs and SIF on mechanism links with GPP, the relationships between EVI and NIR_v with FAPAR, APAR, and APAR$\times$fT$_{min}\times$fVPD are also illustrated in Fig. 6 to investigate whether VIs could explain physiological information of GPP except for structural information. NIR_v and EVI showed strong correlations with FAPAR, APAR, and APAR$\times$fTmin$\times$fVPD. The relationships of the VIs with FAPAR were much stronger than those with APAR, with the highest values of R^2 as 0.73 and 0.74 for EVI and NIR_v, respectively. The relationships strengthened when considering the impact of environmental factors but were still weaker than that with FAPAR, which revealed that EVI and NIR_v mainly contained information on FAPAR and partly accounted for environmental effects.

C. Biome-Specific Relationships Between TanSat SIF and EC GPP

To investigate whether a unique relationship exists between satellite-based SIF and EC GPP across different biomes, we examined the relationships between EC GPP and TanSat SIF at both bands and timescales for nine biomes (see Figs. 7 and 8).

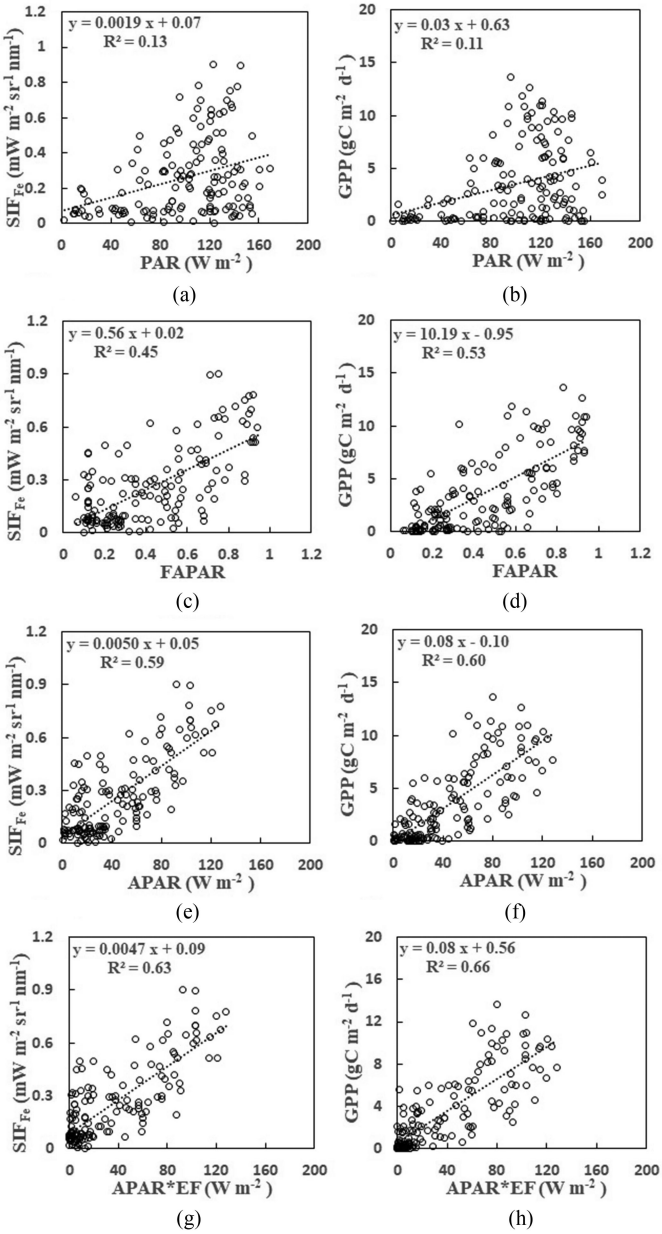

Fig. 5. Relationships between TanSat SIF and GPP with PAR, FAPAR, APAR, and APAR$\times$EF. EF is the product of fT_{min} and fVPD. SIF at Fe band versus (a) PAR, (c) FAPAR, (e) APAR, and (g) APAR$\times$EF. EC GPP versus (b) PAR, (d) FAPAR, (f) APAR, and (h) APAR$\times$EF.

They showed that overall linear correlations between TanSat SIF and EC GPP were found for all nine biomes. For the Fe band, consistently significant relationships between SIF and GPP were observed with R^2 greater than 0.44 at both instantaneous and daily timescales for all biomes except OSH whose R^2 was only 0.11 and 0.17 at instantaneous timescale and daily timescale, respectively. Similarly, the weakest relationships were also found for the OSH biome at the KI band at both instantaneous ($R^2 = 0.18$) and daily ($R^2 = 0.25$) timescales. Further comparison between different timescales showed that for relationships between EC GPP and TanSat SIF at the Fe band for instantaneous timescale, overall weaker goodnesses-of-fit ($R^2 = 0.11$–0.81)

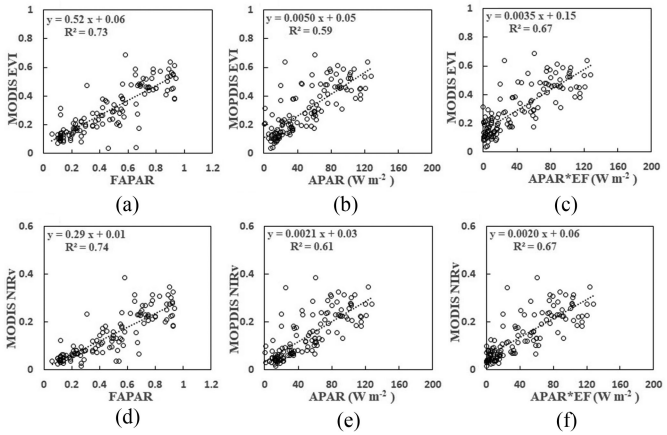

Fig. 6. Relationships between MODIS VIs with FAPAR, APAR, and APAR×EF. EF is the product of fTmin and fVPD. EVI versus (a) FAPAR, (b) APAR, and (c) APAR∗EF. NIR_V versus (d) FAPAR, (e) APAR, and (f) APAR∗EF.

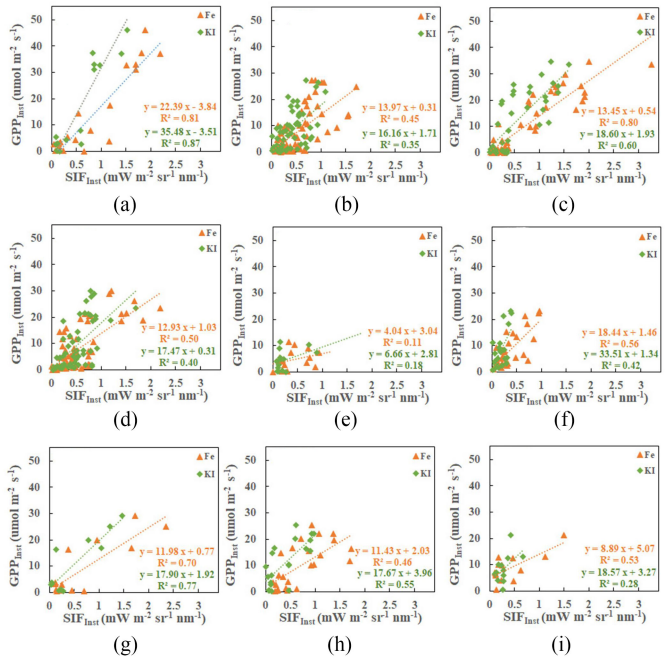

Fig. 7. Relationships between TanSat SIF and EC GPP for nine biomes at both Fe and KI bands for instantaneous timescale. (a) CRO = the cropland type. (b) GRA = grasslands type. (c) DBF = decious broadleaf forests. (d) ENF = evergreen needleleaf forests type. (e) OSH = open shrublands type. (f) SAV = savannas type. (g) MF = mixed forests type. (h) WET = wetlands type. (i) WSA = woody savannas type.

were observed than those of daily timescale (R^2 = 0.17–0.86) for all nine biomes. In addition, the differences in goodness-of-fit were even smaller at the KI band with values of R^2 in the range of 0.18–0.87 and 0.25–0.85 for instantaneous and daily timescales, respectively.

As illustrated in Figs. 7 and 8, the slopes of line relationships were greatest for CRO at Fe band (22.39 μmol·m^{-2}·s^{-1}/mW·m^{-2}·sr^{-1}·nm^{-1} and 20.56 gC·m^{-2}·d^{-1}/mW·m^{-2}·sr^{-1}·nm^{-1} for instantaneous and daily timescales, respectively) and KI band (35.48 μmol·m^{-2}·s^{-1}/

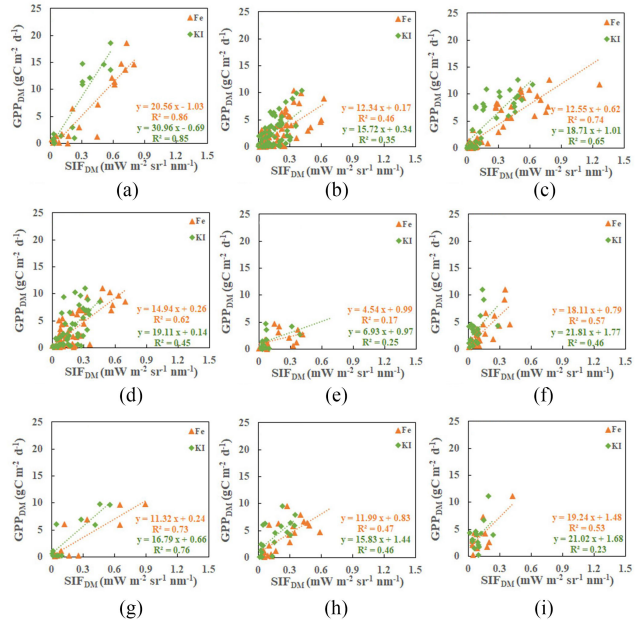

Fig. 8. Relationships between TanSat SIF and EC GPP for nine biomes at both Fe and KI bands for daily timescale. (a) CRO = the cropland type. (b) GRA = grasslands type. (c) DBF = decious broadleaf forests. (d) ENF = evergreen needleleaf forests type. (e) OSH = open shrublands type. (f) SAV = savannas type. (g) MF = mixed forests type. (h) WET = wetlands type. (i) WSA = woody savannas type.

mW·m^{-2}·sr^{-1}·nm^{-1} and 30.96 gC·m^{-2}·d^{-1}/mW·m^{-2}·sr^{-1}·nm^{-1} for instantaneous and daily timescales, respectively) and smallest for OSH with values of the slope of 4.04 μmol·m^{-2}·s^{-1}/mW·m^{-2}·sr^{-1}·nm^{-1} and 4.54 gC·m^{-2}·d^{-1}/mW·m^{-2}·sr^{-1}·nm^{-1} for the Fe band and 6.66 μmol·m^{-2}·s^{-1}/mW·m^{-2}·sr^{-1}·nm^{-1} and 16.93 gC·m^{-2}·d^{-1}/mW·m^{-2}·sr^{-1}·nm^{-1} for the KI band. At Fe and KI bands, the remaining biomes, except for SAV, had relatively similar slopes at instantaneous and daily timescales, respectively. The differences in slopes of the SIF–GPP relationship for all biomes were much smaller at both timescales for the Fe band than for the KI band; only the relationships for CRO and OSHwere significantly different from other biomes for the KI band at both timescales. In general, the slopes of the SIF–GPP relationships were slightly larger at instantaneous timescale than at daily timescale for both bands.

A high correlation between biome-averaged GPP and averaged SIF across nine biomes was observed, as shown in Fig. 9. Similar to the results of Fig. 2, the SIF–GPP relationship at daily time scale (R^2 = 0.76 and 0.65 at Fe and KI bands, respectively) was stronger than at instantaneous timescale (R^2 = 0.73 and 0.63 at Fe and KI bands, respectively). In addition, Fig. 9 shows the remarkable advantages of SIF at Fe band on GPP estimation across biomes.

D. Evaluating the Performance of Satellite SIF on Estimating GPP

The performance of satellite-based SIF on estimating GPP using the SIF-GPP relationship derived from TanSat SIF at the

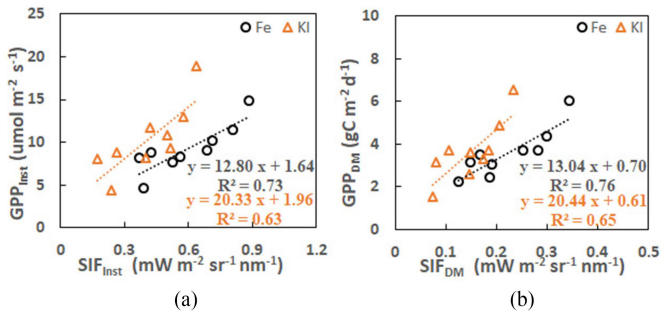

(a) (b)

Fig. 9. Scatter plot of biome-averaged TanSat SIF and EC GPP data for nine biomes at Fe and KI bands for (a) Instantaneous and (b) Daily timescales.

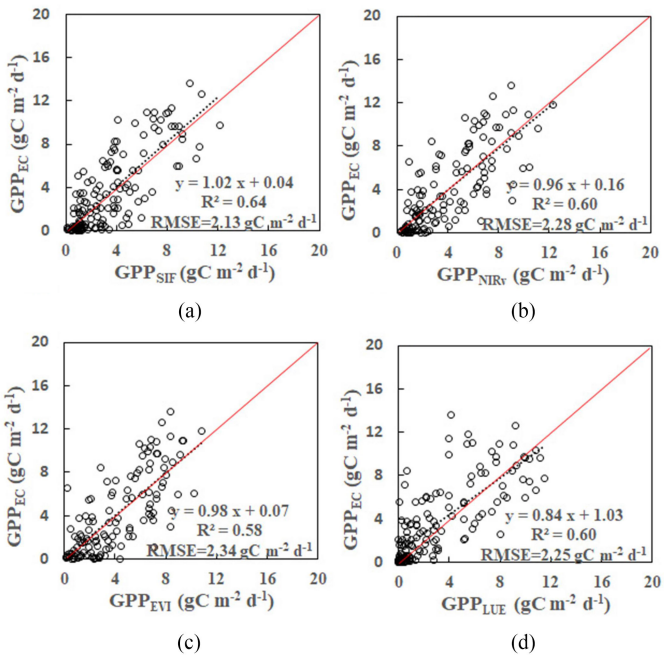

(a) (b) (c) (d)

Fig. 10. Comparisons between EC GPP and estimated GPP derived from linear relationships between EC GPP and (a) TanSat SIF. (b) MODIS NIRv. (c) EVI. and (d) LUE model (MODIS GPP algorithm).

Fe band and EC GPP for different biomes was evaluated using a ten-fold cross-validation approach. Considering the availability of auxiliary data used in the LUE model and the consistency of datasets used for four models, the validation dataset used was slightly less than that in Fig. 2. The overall good correspondence between EC GPP and GPP estimates could be observed (see Fig. 10). From Fig. 10(a), the SIF-based GPP estimates derived from TanSat data at the Fe band had a good linear relationship with EC GPP (R^2 = 0.64, RMSE = 2.13 gC·m^{-2}·d^{-1}) with all the points lying near the 1:1 line, indicating a high degree of consistency between them. Besides the SIF-based GPP estimates, we also performed GPP estimation using a VI-based algorithm and the traditional LUE-based model (MODIS GPP algorithm). The GPP estimates based on NIR$_v$ had comparable performances to the MODIS GPP algorithm with R^2 of both as 0.60 and RMSE of 2.28 and 2.25 gC·m^{-2}·d^{-1} for NIR$_v$ and MODIS GPP algorithm, respectively. However, the scatter plots of the relationship between EC GPP and GPP estimates based on the MODIS GPP algorithm were more discrete. EVI performed slightly worse than NIR$_v$ and MODIS algorithm as well as SIF with R^2 of 0.58 and the highest RMSE of 2.34 gC·m^{-2}·d^{-1}. In general, VI-based and MODIS GPP algorithms slightly underestimated GPP, especially at high values of GPP. Overall, the results showed that satellite-based SIF could be used for GPP estimation slightly better than VI-based and MODIS GPP algorithm.

IV. Discussion

Previous studies have demonstrated significant relationships between GOME-2 or GOSAT SIF and gridded GPP [9], [11], [21], [52]. However, owing to the uncertainties of gridded GPP and coarse spatial resolutions of GOME-2 and GOSAT, direct comparison between GOSAT and GOME-2 SIF products with EC flux GPP has been hindered. In general, the spatial scale mismatch was a key difficulty in validating or comparing satellite-based remote sensing products with ground observations. Afterward, OCO-2 provided the first opportunity for evaluating the relationship between satellite SIF and EC flux GPP observations due to its fine spatial resolution of 1.3 km ×2.25 km [37]. In addition, several studies have employed OCO-2 SIF to investigate the relationship with flux tower GPP and found strong correlations between them [41], [42]. Similarly, it is possible to evaluate TanSat SIF using EC flux GPP with a 2-km spatial resolution. Such fine spatial resolution has advantages in matching satellites with tower footprint and conducting a site-scale analysis for satellite SIF with tower GPP.

Our results showed that strong correlations between TanSat SIF and EC GPP were observed at the Fe and KI bands for instantaneous and daily timescales. In addition, the relationship of GPP with SIF$_{Fe}$ was much stronger than SIF$_{KI}$, whereas no significant distinctions on the relationship for instantaneous and daily timescales were observed. Previous works have found the stronger ability of SIF$_{Fe}$ on estimating GPP than that of SIF$_{KI}$ [41], [42], which was attributed to the much stronger signal of SIF$_{Fe}$ than SIF$_{KI}$. In general, the signals of SIF$_{Fe}$ was 1.4–1.7 times higher than that of SIF$_{KI}$ [38]. On the one hand, SIF$_{Fe}$ is closer to the far-red peak of SIF spectrum; on the other hand, the depth of Fraunhofer line at Fe band was much deeper than that at KI band, resulting more uncertainties in SIF retrievals at KI band than that at Fe band. Extensive previous studies have investigated the relationships between SIF and GPP. Generally, most studies reported linear relationships between SIF and GPP based on simulated datasets [53], [54], ground measurements [16], and satellite-based observations [9], [11], [21], [55]. By contrast, some studies also demonstrated that the nonlinear relationships existed between SIF and GPP at the instantaneous timescale or leaf scale [17], [19], and the relationships would be linear when SIF and GPP were at the canopy level or aggregated to daily timescale or other longer timescales. However, our global analysis showed obvious linear relationships between TanSat SIF and EC GPP even at an instantaneous timescale. Except for daily timescale, the differences in accuracy between linear and nonlinear models were even negligible at instantaneous timescale, which was seemingly contradictory with the previous

conclusions [17], [19]. This may result from the limited available satellite-based data soundings that matched with EC observations. In fact, the mechanistic and complex relationship between satellite SIF and EC GPP would be affected by many factors, such as light conditions, canopy or leaf structures, physiological responses, scale effects, and environmental factors [56], [57]. Therefore, how linear or nonlinear relationships are presented need more available measurements covering different temporal and spatial scales and further investigation in the future work.

Strong relationships between TanSat SIF and EC GPP were observed in eight of the nine biomes at both bands. The weakest relationships occurred in the OSH with R^2 ranging from 0.11 to 0.25. No significant differences in slopes of relationships between TanSat SIF and EC GPP were found, except for CRO and OSH biomes, especially for the Fe band, which was seemingly contradictory with previous works showing that the relationships between satellite SIF and GPP depended on vegetation biomes [21], [22], [31], [52], [58]. However, the biome-dependent SIF-GPP relationships may be slightly larger for the KI band. In fact, the biome-specific findings of the SIF–GPP relationships were mostly concluded from either GOME-2 SIF with coarse-spatial resolution or gridded GPP estimates with large estimated uncertainties. Previous studies have also found similar relationships between satellite SIF and GPP using OCO-2 SIF and individual or amount of EC flux GPP observations [23], [41]. Sun *et al.* found that crops, forest, and grass had similar slopes using limited concurrent observations (∼30 samples) of OCO-2 SIF and EC tower GPP [23]. Similarly, Li *et al.* also observed similar slopes in SIF-GPP relationship using OCO-2 SIF_{757} and tower GPP based on 64 sites, and the smallest slope was observed in EBF [41]. However, our results showed that the value of slope in CRO was much larger than forest biome and the weakest relationship and smallest slope were occurred in OSH. These could largely result from the differences in available concurrent satellite dataset used in comparison with EC GPP and the spatial heterogeneity in different EC sites. In our results, the uncertainties of OSH may result from the very limited number of TanSat observations (less than 20 samples) overpassing EC flux site for OSH biome with EC GPP ranging from 0 to 11.3 $\mu mol \cdot m^{-2} \cdot s^{-1}$ at instantaneous timescale and from 0.04 to 4.65 $gC \cdot m^{-2} \cdot d^{-1}$ for daily timescale for the matched samples. Therefore, the slopes and relationships for OSH may be altered if more valid matched samples are available. As for CRO, previous works have demonstrated that the canopy structure has a strong impact on the SIF–GPP relationship in crops [19], [20]. Moreover, photosynthetic pathways will affect the slopes of the SIF–GPP relationship. Liu *et al.* [54] reported that C_4 crops had a higher slope than C_3 type based on ground measurements. Therefore, the differences in slopes of SIF-GPP relationship for CRO require further studies.

To help evaluate the capability of TanSat SIF on estimating GPP, we examined the relationships between EC GPP and MODIS-derived NDVI, EVI, and NIR_v. Previous works have shown that satellite SIF correlated more with nadir BRDF-adjusted VIs than that derived from Terra or Aqua reflectance due to the effects of varying observation geometry on reflectance [41]. So, VIs calculated from MODIS BRDF-corrected reflectance were used for comparisons, and we found stronger relationships between EVI, $NIR_{v,}$ and EC GPP than NDVI but still slightly weaker than that for TanSat SIF. The result agreed with previous results, showing that SIF could better characterize the actual photosynthesis than traditional VIs [4]–[6]. The examination of the relationships between EVI or NIR_v and FAPAR showed their relationships were also better than that of EVI, $NIR_{v,}$ and SIF or GPP, demonstrating that traditional VIs were great proxies for FAPAR, especially for EVI and NIR_v. Unlike VIs, SIF could account for information on instantaneous illumination, leading to sensitivity to rapid changes in physiology [15]. However, NIR_v presented similarly strong relationships with EC GPP and TanSat SIF, indicating that BRDF-corrected NIR_v derived from MODIS also have strong predictive ability for estimating GPP, consistent with that NIR_v could be regarded as a direct index of photons intercepted by chlorophyll [59]. Moreover, we observed the saturation phenomenon of relationships between SIF or GPP and NDVI, which contributes to the saturation of NDVI at high LAI [62]. So, EVI and NIR_v largely eliminated this disadvantage for dense vegetation. Meanwhile, the MODIS-derived NIR_v could be easily available and even more spatially and temporally continuous compared to SIF [59]–[61]. From this perspective, NIR_v could also be used for estimates of GPP at site level or global scale and has unique advantages on data amount.

To further reveal the mechanisms underlying the SIF–GPP relationship, we investigated how SIF and EC GPP responded to APAR, respectively. Many previous studies suggested that the SIF–GPP relationship was dominated by APAR [63], whereas a recent study highlighted the dominant role of canopy structure in the SIF–GPP relationship for CRO biome [20]. Our results showed much higher correlations between TanSat SIF, EC GPP, and APAR compared to PAR. Moreover, except for APAR, we found that SIF responded to environmental factors (fTmin and fVPD) similar to GPP. The correlations between the products of these two environmental factors and APAR explained more variances of TanSat SIF and EC GPP than APAR alone. Several previous works also identified environmental control factors influencing both SIF and GPP using GOME-2 and OCO-2 SIF observations [41], [64]. Low air temperature and VPD could regulate photosynthesis ability by affecting the effective maximum rate of carboxylation and stomatal conductance and intercellular CO2 concentration, respectively, which result in LUE_p variation. The results of this study showed that the LUE_p determination could also influence SIF, which indicated the mechanism foundation of the application of SIF on estimating GPP. However, how SIF_{yield} or f_{esc} respond to LUE_p requires further investigation.

Our comparisons of estimated GPP based on the SIF and LUE model showed the predictive ability of SIF was slightly better than the MODIS GPP algorithm. A series of ancillary variables, including PAR and FAPAR, and different environmental factors, as well as biome classification products, were required in the MODIS GPP algorithm. However, these variables used in the MODIS GPP model have significant uncertainties [65], which will lead to large uncertainties on GPP estimations. Moreover, previous works have demonstrated the underestimation of

MODIS GPP compared with EC GPP. Unlike the LUE model, the GPP estimated method based on SIF does not need the above ancillary dataset, which will reduce uncertainties in the GPP estimation of the LUE-based model. Meanwhile, SIF has excellent performance on estimating GPP, thus could potentially be widely used in further carbon cycling works.

Despite the great performance of SIF on estimating GPP, the wide application of TanSat SIF on regional or global GPP estimation is still challenging. First, it is extremely difficult to obtain long-term continuous and wide-spatial coverage of TanSat SIF due to the spatially and temporally sparse coverage of TanSat. On one hand, only TanSat SIF products at nadir mode were successfully retrieved due to the quality problem of data in the glint mode, which result in the reduction of approximately half of the TanSat data available. It was difficult to generate gridded SIF at high spatial and temporal resolutions. On the other hand, TanSat data have not been available since November 2019 due to the instrument breakdown. Second, the available number of EC flux data for most sites is limited and the public datasets also have significant uncertainties, especially for a missing problem. Therefore, only a few TanSat SIF observations were available for most EC flux sites over the globe in this study. It was impossible to conduct seasonal and even interannual analyses in vegetation photosynthesis or phenology at the site scale and examine the relationships over space. Further examinations of the relationship between TanSat SIF and EC GPP will need more available matched soundings for several vegetation biomes, such as OSH and SAV. One solution is to expect that more EC flux datasets could be public in the future. Another possible solution is to incorporate other spatially and temporally continuous satellite datasets, e.g., MODIS, GOME-2 and TROPOMI SIF products, with TanSat SIF to generate continuous SIF estimates based on machine learning algorithm [66].

V. Conclusion

We have used the nearly concurrent TanSat SIF and global EC flux observations (March 2017 to December 2019) encompassing 129 EC flux sites and covering 9 major vegetation biomes to analyze the relationship between satellite-based SIF and EC GPP at two bands (Fe and KI) for two timescales (instantaneous and daily). Significant relationships between TanSat SIF and EC GPP were observed at both Fe and KI bands for instantaneous and daily timescales with much stronger relationships at the Fe band than the KI band. EC GPP was more strongly correlated with TanSat SIF at Fe band ($R^2 = 0.61$) than MODIS-derived BRDF-corrected NDVI ($R^2 = 0.49$) and slightly better than with BRDF-corrected EVI ($R^2 = 0.54$) and NIR_v ($R^2 = 0.58$). We further investigated the responses of TanSat SIF and EC GPP to APAR and two environmental factors and found that SIF was dominated by APAR and also influenced by environmental factors similar to GPP. Strong correlations between TanSat SIF and EC GPP were shown for all biomes except for OSH ($R^2 = 0.11$–0.25), and a consistent relationship was observed across nine biomes except for CRO and OSH with much higher and lower slopes, respectively. The GPP estimates based on SIF performed better than those based on EVI and NIR_v as well as the MODIS GPP algorithm. Therefore, TanSat provides an unprecedented SIF dataset comparable to ground-based EC measurements with fine spatial resolution. In addition, we demonstrated the predictive ability of TanSat SIF on estimating GPP. Combining TanSat SIF having fine spatial resolution with other satellite SIF products (e.g., GOME-2, TROPOMI, OCO-2, and FLEX) will be helpful for future carbon cycling studies.

Acknowledgment

The authors would like to acknowledge the AmeriFlux Network and National Tibetan Plateau Third Pole Environment Data Center for making the EC flux data public, and Prof. Shaomin Liu and Dr. Ziwei Xu at Beijing Normal University and Yongguang, Zhang for providing the flux datasets. The authors would also like to thank the MODIS data processing team for making available the MODIS data. All the MODIS data were obtained from the NASA Level-1 and Atmosphere Archive and Distribution System Distributed Active Archive Center (LAADS DAAC).

References

[1] C. Beer *et al.*, "Terrestrial gross carbon dioxide uptake: Global distribution and covariation with climate," *Science*, vol. 329, no. 5993, pp. 834–838, 2010.

[2] G. Duveiller and A. Cescatti, "Spatially downscaling sun-induced chlorophyll fluorescence leads to an improved temporal correlation with gross primary productivity," *Remote Sens. Environ.*, vol. 182, pp. 72–89, 2016, doi: 10.1016/j.rse.2016.04.027.

[3] J. Xiao *et al.*, "Twentieth-century droughts and their impacts on terrestrial carbon cycling in China," *Earth Interact.*, vol. 13, no. 10, pp. 1–31, 2009, doi: 10.1175/2009ei275.1.

[4] W. Yuan *et al.*, "Global estimates of evapotranspiration and gross primary production based on MODIS and global meteorology data," *Remote Sens. Environ.*, vol. 114, no. 7, pp. 1416–1431, 2010.

[5] A. D. Richardson *et al.*, "Terrestrial biosphere models need better representation of vegetation phenology: Results from the North American carbon program site synthesis," *Global Change Biol.*, vol. 18, no. 2, pp. 566–584, 2012.

[6] D. P. Turner *et al.*, "Evaluation of MODIS NPP and GPP products across multiple biomes," *Remote Sens. Environ.*, vol. 102, no. 3/4, pp. 282–292, 2006.

[7] J. A. Gamon, O. Kovalchuck, C. Y. S. Wong, A. Harris, and S. R. Garrity, "Monitoring seasonal and diurnal changes in photosynthetic pigments with automated PRI and NDVI sensors," *Biogeosciences*, vol. 12, no. 13, pp. 4149–4159, 2015, doi: 10.5194/bg-12-4149-2015.

[8] O. Perez-Priego *et al.*, "Sun-induced chlorophyll fluorescence and photochemical reflectance index improve remote-sensing gross primary production estimates under varying nutrient availability in a typical Mediterranean Savanna ecosystem," *Biogeosciences*, vol. 12, no. 21, pp. 6351–6367, 2015.

[9] L. Guanter *et al.*, "Global and time-resolved monitoring of crop photosynthesis with chlorophyll fluorescence," *Proc. Nat. Acad. Sci. USA*, vol. 111, no. 14, pp. E1327–E1333, 2014, doi: 10.1073/pnas.1320008111.

[10] J. Joiner *et al.*, "The seasonal cycle of satellite chlorophyll fluorescence observations and its relationship to vegetation phenology and ecosystem atmosphere carbon exchange," *Remote Sens. Environ.*, vol. 152, pp. 375–391, 2014.

[11] C. Frankenberg *et al.*, "New global observations of the terrestrial carbon cycle from GOSAT: Patterns of plant fluorescence with gross primary productivity," *Geophys. Res. Lett.*, vol. 38, no. 17, 2011, Art. no. L17706, doi: 10.1029/2011gl048738.

[12] A. Porcar-Castell *et al.*, "Linking chlorophyll a fluorescence to photosynthesis for remote sensing applications: Mechanisms and challenges," *J. Exp. Botany*, vol. 65, no. 15, pp. 4065–4095, 2014, doi: 10.1093/jxb/eru191.

[13] P. J. Zarco-Tejada, J. Pushnik, S. Dobrowski, and S. L. Ustin, "Steady-state chlorophyll a fluorescence detection from canopy derivative reflectance and double-peak red-edge effects," *Remote Sens. Environ.*, vol. 84, no. 2, pp. 283–294, 2003.

[14] M. Meroni *et al.*, "Remote sensing of solar-induced chlorophyll fluorescence: Review of methods and applications," *Remote Sens. Environ.*, vol. 113, no. 10, pp. 2037–2051, 2009, doi: 10.1016/j.rse.2009.05.003.

[15] P. J. Zarco-Tejada, A. Morales, L. Testi, and F. J. Villalobos, "Spatio-temporal patterns of chlorophyll fluorescence and physiological and structural indices acquired from hyperspectral imagery as compared with carbon fluxes measured with eddy covariance," *Remote Sens. Environ.*, vol. 133, pp. 102–115, 2013.

[16] T. S. Magney *et al.*, "Mechanistic evidence for tracking the seasonality of photosynthesis with solar-induced fluorescence," *Proc. Nat. Acad. Sci. USA*, vol. 116, no. 24, pp. 11640–11645, Jun. 2019, doi: 10.1073/pnas.1900278116.

[17] A. Damm *et al.*, "Far-red sun-induced chlorophyll fluorescence shows ecosystem-specific relationships to gross primary production: An assessment based on observational and modeling approaches," *Remote Sens. Environ.*, vol. 166, pp. 91–105, 2015, doi: 10.1016/j.rse.2015.06.004.

[18] Z. Liu, X. Lu, S. An, M. Heskel, H. Yang, and J. Tang, "Advantage of multi-band solar-induced chlorophyll fluorescence to derive canopy photosynthesis in a temperate forest," *Agric. Forest Meteorol.*, vol. 279, 2019, Art. no. 107691, doi: 10.1016/j.agrformet.2019.107691.

[19] Z. Li *et al.*, "Solar-induced chlorophyll fluorescence and its link to canopy photosynthesis in maize from continuous ground measurements," *Remote Sens. Environ.*, vol. 236, 2020, Art. no. 111420, doi: 10.1016/j.rse.2019.111420.

[20] B. Dechant *et al.*, "Canopy structure explains the relationship between photosynthesis and sun-induced chlorophyll fluorescence in crops," *Remote Sens. Environ.*, vol. 241, 2019, Art. no. 111733.

[21] Y. Zhang *et al.*, "Consistency between sun-induced chlorophyll fluorescence and gross primary production of vegetation in North America," *Remote Sens. Environ.*, vol. 183, pp. 154–169, 2016, doi: 10.1016/j.rse.2016.05.015.

[22] Y. Sun *et al.*, "Overview of solar-induced chlorophyll fluorescence (SIF) from the orbiting carbon observatory-2: Retrieval, cross-mission comparison, and global monitoring for GPP," *Remote Sens. Environ.*, vol. 209, pp. 808–823, 2018, doi: 10.1016/j.rse.2018.02.016.

[23] Y. Sun *et al.*, "OCO-2 advances photosynthesis observation from space via solar-induced chlorophyll fluorescence," *Science*, vol. 358, no. 6360, Oct. 2017, doi: 10.1126/science.aam5747.

[24] H. Wang and J. Xiao, "Improving the capability of the SCOPE model for simulating solar-induced fluorescence and gross primary production using data from OCO-2 and flux towers," *Remote Sens.*, vol. 13, no. 4, 2021, Art. no. 794, doi: 10.3390/rs13040794.

[25] X. Liu, L. Liu, J. Hu, and S. Du, "Modeling the footprint and equivalent radiance transfer path length for tower-based hemispherical observations of chlorophyll fluorescence," *Sensors*, vol. 17, no. 5, May 2017, Art. no. 1131, doi: 10.3390/s17051131.

[26] A. Porcar-Castell *et al.*, "EUROSPEC: At the interface between remote-sensing and ecosystem CO2 flux measurements in Europe," *Biogeosciences*, vol. 12, no. 20, pp. 6103–6124, 2015, doi: 10.5194/bg-12-6103-2015.

[27] J. Joiner *et al.*, "Global monitoring of terrestrial chlorophyll fluorescence from moderate-spectral-resolution near-infrared satellite measurements: Methodology, simulations, and application to GOME-2," *Atmos. Meas. Techn.*, vol. 6, no. 10, pp. 2803–2823, 2013, doi: 10.5194/amt-6-2803-2013.

[28] J. Joiner, Y. Yoshida, L. Guanter, and E. M. Middleton, "New methods for the retrieval of chlorophyll red fluorescence from hyperspectral satellite instruments: Simulations and application to GOME-2 and SCIAMACHY," *Atmos. Meas. Techn.*, vol. 9, no. 8, pp. 3939–3967, 2016, doi: 10.5194/amt-9-3939-2016.

[29] J. Joiner *et al.*, "Filling-in of far-red and near-infrared solar lines by terrestrial and atmospheric effects: Simulations and space-based observations from SCIAMACHY and GOSAT," *Atmos. Meas. Techn. Discuss.*, vol. 5, no. 1, pp. 163–210, 2012, doi: 10.5194/amtd-5-163-2012.

[30] P. Köhler, L. Guanter, and J. Joiner, "A linear method for the retrieval of sun-induced chlorophyll fluorescence from GOME-2 and SCIAMACHY data," *Atmos. Meas. Techn.*, vol. 8, no. 6, pp. 2589–2608, 2015, doi: 10.5194/amt-8-2589-2015.

[31] L. Guanter *et al.*, "Retrieval and global assessment of terrestrial chlorophyll fluorescence from GOSAT space measurements," *Remote Sens. Environ.*, vol. 121, pp. 236–251, 2012, doi: 10.1016/j.rse.2012.02.006.

[32] C. Frankenberg, A. Butz, and G. C. Toon, "Disentangling chlorophyll fluorescence from atmospheric scattering effects in O2A-band spectra of reflected sun-light," *Geophys. Res. Lett.*, vol. 38, no. 3, 2011, Art. no. L03801, doi: 10.1029/2010gl045896.

[33] P. Kohler, L. Guanter, and C. Frankenberg, "Simplified physically based retrieval of sun-induced chlorophyll fluorescence from GOSAT data," *IEEE Geosci. Remote Sens. Lett.*, vol. 12, no. 7, pp. 1446–1450, Jul. 2015.

[34] P. Köhler, C. Frankenberg, T. S. Magney, L. Guanter, J. Joiner, and J. Landgraf, "Global retrievals of solar-induced chlorophyll fluorescence with TROPOMI: First results and intersensor comparison to OCO-2," *Geophys. Res. Lett.*, vol. 45, no. 19, pp. 10456–10463, 2018, doi: 10.1029/2018gl079031.

[35] P. Köhler, M. J. Behrenfeld, J. Landgraf, J. Joiner, T. S. Magney, and C. Frankenberg, "Global retrievals of solar-induced chlorophyll fluorescence at red wavelengths with TROPOMI," *Geophys. Res. Lett.*, vol. 47, no. 15, 2020, Art. no. e2020GL087541, doi: 10.1029/2020gl087541.

[36] L. Guanter *et al.*, "Potential of the TROPOspheric monitoring instrument (TROPOMI) onboard the sentinel-5 precursor for the monitoring of terrestrial chlorophyll fluorescence," *Atmos. Meas. Techn.*, vol. 8, no. 3, pp. 1337–1352, 2015, doi: 10.5194/amt-8-1337-2015.

[37] C. Frankenberg *et al.*, "The orbiting carbon observatory (OCO-2): Spectrometer performance evaluation using pre-launch direct sun measurements," *Atmos. Meas. Techn. Discuss.*, vol. 7, no. 7, pp. 7641–7670, 2014, doi: 10.5194/amtd-7-7641-2014.

[38] C. Frankenberg, C. Dell, and L. Guanter, "Prospects for chlorophyll fluorescence remote sensing from the orbiting carbon Observatory-2," *Remote Sens. Environ.*, vol. 147, pp. 1–12, 2014.

[39] S. Du *et al.*, "Retrieval of global terrestrial solar-induced chlorophyll fluorescence from TanSat satellite," *Sci. Bull.*, vol. 63, no. 22, pp. 1502–1512, 2018, doi: 10.1016/j.scib.2018.10.003.

[40] Z. Yang *et al.*, "Laboratory spectral calibration of the TanSat atmospheric carbon dioxide grating spectrometer," *Geosci. Instrum., Methods Data Syst.*, vol. 7, no. 3, 2018, Art. no. 245.

[41] X. Li, J. Xiao, and B. He, "Chlorophyll fluorescence observed by OCO-2 is strongly related to gross primary productivity estimated from flux towers in temperate forests," *Remote Sens. Environ.*, vol. 204, pp. 659–671, 2018, doi: 10.1016/j.rse.2017.09.034.

[42] X. Li *et al.*, "Solar-induced chlorophyll fluorescence is strongly correlated with terrestrial photosynthesis for a wide variety of biomes: First global analysis based on OCO-2 and flux tower observations," *Global Change Biol*, vol. 24, no. 9, pp. 3990–4008, Sep. 2018, doi: 10.1111/gcb.14297.

[43] X. Lu, X. Cheng, X. Li, and J. Tang, "Opportunities and challenges of applications of satellite-derived sun-induced fluorescence at relatively high spatial resolution," *Sci. Total Environ.*, vol. 619/620, pp. 649–653, Apr. 2018, doi: 10.1016/j.scitotenv.2017.11.158.

[44] Y. Liu *et al.*, "The TanSat mission: Preliminary global observations," *Sci. Bull.*, vol. 63, no. 18, pp. 1200–1207, 2018, doi: 10.1016/j.scib.2018.08.004.

[45] S. M. Liu *et al.*, "A comparison of eddy-covariance and large aperture scintillometer measurements with respect to the energy balance closure problem," *Hydrol. Earth Syst. Sci.*, vol. 15, no. 4, pp. 1291–1306, 2011.

[46] S. Liu *et al.*, "The Heihe integrated observatory network: A basin-scale land surface processes observatory in China," *Vadose Zone J.*, vol. 17, no. 1, pp. 1–21, 2018.

[47] D. Papale *et al.*, "Towards a standardized processing of net ecosystem exchange measured with eddy covariance technique: Algorithms and uncertainty estimation," *Biogeosciences*, vol. 3, no. 4, pp. 571–583, 2006.

[48] D. Baldocchi *et al.*, "FLUXNET: A new tool to study the temporal and spatial variability of ecosystem-scale carbon dioxide, water vapor, and energy flux densities," *Bull. Amer. Meteorol. Soc.*, vol. 82, no. 11, pp. 2415–2434, 2001.

[49] M. Reichstein *et al.*, "On the separation of net ecosystem exchange into assimilation and ecosystem respiration: Review and improved algorithm," *Global Change Biol.*, vol. 11, no. 9, pp. 1424–1439, 2005, doi: 10.1111/j.1365-2486.2005.001002.x.

[50] G. Lasslop *et al.*, "Separation of net ecosystem exchange into assimilation and respiration using a light response curve approach: Critical issues and global evaluation," *Global Change Biol.*, vol. 16, no. 1, pp. 187–208, 2010.

[51] A. R. Desai *et al.*, "Cross-site evaluation of eddy covariance GPP and RE decomposition techniques," *Agric. Forest Meteorol.*, vol. 148, no. 6/7, pp. 821–838, 2008.

[52] Y. Zhang *et al.*, "Model-based analysis of the relationship between sun-induced chlorophyll fluorescence and gross primary production for remote sensing applications," *Remote Sens. Environ.*, vol. 187, pp. 145–155, 2016, doi: 10.1016/j.rse.2016.10.016.

[53] M. Migliavacca *et al.*, "Plant functional traits and canopy structure control the relationship between photosynthetic CO2 uptake and far-red sun-induced fluorescence in a Mediterranean grassland under different nutrient availability," *New Phytologist*, vol. 214, no. 3, pp. 1078–1091, 2017.
[54] L. Liu, L. Guan, and X. Liu, "Directly estimating diurnal changes in GPP for C3 and C4 crops using far-red sun-induced chlorophyll fluorescence," *Agric. Forest Meteorol.*, vol. 232, pp. 1–9, 2017, doi: 10.1016/j.agrformet.2016.06.014.
[55] Y. Zhang *et al.*, "On the relationship between sub-daily instantaneous and daily total gross primary production: Implications for interpreting satellite-based SIF retrievals," *Remote Sens. Environ.*, vol. 205, pp. 276–289, 2018, doi: 10.1016/j.rse.2017.12.009.
[56] M. Verma *et al.*, "Effect of environmental conditions on the relationship between solar-induced fluorescence and gross primary productivity at an Ozflux grassland site," *J. Geophys. Res., Biogeosci.*, vol. 122, no. 3, pp. 716–733, 2017.
[57] H. Yang *et al.*, "Chlorophyll fluorescence tracks seasonal variations of photosynthesis from leaf to canopy in a temperate forest," *Global Change Biol.*, vol. 23, no. 7, pp. 2874–2886, Jul. 2017, doi: 10.1111/gcb.13590.
[58] N. C. Parazoo *et al.*, "Terrestrial gross primary production inferred from satellite fluorescence and vegetation models," *Global Change Biol.*, vol. 20, no. 10, pp. 3103–3121, 2014.
[59] G. Badgley, C. B. Field, and J. A. Berry, "Canopy near-infrared reflectance and terrestrial photosynthesis," *Sci. Adv.*, vol. 3, no. 3, 2017, Art. no. e1602244.
[60] G. Badgley, L. D. Anderegg, J. A. Berry, and C. B. Field, "Terrestrial gross primary production: Using NIRV to scale from site to globe," *Global Change Biol.*, vol. 25, no. 11, pp. 3731–3740, 2019.
[61] S. Wang, Y. Zhang, W. Ju, B. Qiu, and Z. Zhang, "Tracking the seasonal and inter-annual variations of global gross primary production during last four decades using satellite near-infrared reflectance data," *Sci. Total Environ.*, vol. 755, 2021, Art. no. 142569.
[62] A. Nguy-Robertson, A. Gitelson, Y. Peng, A. Viña, T. Arkebauer, and D. Rundquist, "Green leaf area index estimation in maize and soybean: Combining vegetation indices to achieve maximal sensitivity," *Agronomy J.*, vol. 104, no. 5, pp. 1336–1347, 2012.
[63] S. Du, L. Liu, X. Liu, and J. Hu, "Response of canopy solar-induced chlorophyll fluorescence to the absorbed photosynthetically active radiation absorbed by chlorophyll," *Remote Sens.*, vol. 9, no. 9, Sep. 2017, Art. no. 911, doi: 10.3390/rs9090911.
[64] N. Madani, J. S. Kimball, L. A. Jones, N. C. Parazoo, and K. Guan, "Global analysis of bioclimatic controls on ecosystem productivity using satellite observations of solar-induced chlorophyll fluorescence," *Remote Sens.*, vol. 9, no. 6, 2017, Art. no. 530.
[65] M. Zhao, S. W. Running, and R. R. Nemani, "Sensitivity of moderate resolution imaging spectroradiometer (MODIS) terrestrial primary production to the accuracy of meteorological reanalyses," *J. Geophys. Res., Biogeosci.*, vol. 111, 2006, Art. no. G1.
[66] Y. Ma, L. Liu, R. Chen, S. Du, and X. Liu, "Generation of a global spatially continuous TanSat solar-induced chlorophyll fluorescence product by considering the impact of the solar radiation intensity," *Remote Sens.*, vol. 12, no. 13, 2020, Art. no. 2167.

Shanshan Du received the Ph.D. degree in cartography and geographic information system from Aerospace Information Research Institute, Chinese Academy of Sciences, Beijing, China, in 2020.

She is a Postdoctoral Researcher with Aerospace Information Research Institute, Chinese Academy of Sciences. Her research interests include retrieval and application of solar-induced chlorophyll fluorescence based on satellite observations.

Liangyun Liu received the Ph.D. degree in optical engineering from Xi'an Institute of Optical and Precision Mechanics, Chinese Academy of Sciences, Xi an, China, in 2000.

He is currently a Professor with Aerospace Information Research Institute, Chinese Academy of Sciences, Beijing, China. His research focuses on quantitative remote sensing of vegetation.

Xinjie Liu received the Ph.D. degree in cartography and geographic information system from the Institute of Remote Sensing and Digital Earth, Chinese Academy of Sciences, Beijing, China, in 2016.

He is currently an Associate Professor with the Aerospace Information Research Institute, Chinese Academy of Sciences, Beijing, China. His current research focuses on remote sensing of solar-induced chlorophyll fluorescence.

Jidai Chen received the master's degree from Beijing Forestry University, Beijing, China, in 2019. He is currently working toward the Ph.D. degree with the Aerospace Information Research Institute, Chinese Academy of Sciences, Beijing, China.

His research interests include the application of solar-induced chlorophyll fluorescence, gross primary production, and the environmental stress.